Method for high precision measurement of decaying dynamics using attosecond wave-mixing spectroscopy

KANG MI,[1] WEI CAO,[1,*] HUIYAO XU,[1] QINGBIN ZHANG,[1,3] AND PEIXIANG LU[1,2,4]

[1]*School of Physics and Wuhan National Laboratory for Optoelectronics, Huazhong University of Science and Technology, Wuhan 430074, China*
[2]*Hubei Key Laboratory of Optical Information and Pattern Recognition, Wuhan Institute of Technology, Wuhan 430205, China*
[3]*zhangqingbin@hust.edu.cn*
[4]*lupeixiang@mail.hust.edu.cn*
[*]*weicao@hust.edu.cn*

Abstract: Ultrafast wave-mixing spectroscopies involving extreme ultraviolet (EUV) attosecond pulses provide unprecedented insight into electronic dynamics. Here, we proposed a versatile lifetime-detection method for doubly excited states with odd or even parities by mixing an attosecond EUV pulse with two few-cycle near infrared (NIR) pulses in atomic helium under a noncollinear geometry. By properly choosing the time order of the pulse sequence, the spatially resolved nonlinear signals carry significant information of the decaying dynamics of excited states, which can be utilized to retrieve the lifetimes of states with different parities in a single measurement. The validity and robustness of the method has been verified by numerical simulations based on a few-level model of helium including the spatial distribution of atoms. The accuracy of the lifetime measurement method is better than a few hundred attoseconds. It provides a powerful tool for probing decaying dynamics of the electronic wave packet with superb resolution.

1. Introduction

Excited electrons will either decay to the state with lower energy via radiative decay or autoionize via electronic rearrangement [1,2]. The time scale of the decay process is associated with the lifetime of corresponding excited state. At the beginning, the excited-state lifetimes are deduced from the measured line widths of the static absorption features, by using synchrotron radiation facilities [3]. However, various possible broadening mechanisms may complicate lifetime measurement [4]. To overcome the limitation of static absorption methods, time-domain measurement of decaying process has been proposed accompanied by the emergence of ultrashort light sources with pulse duration on the order of femtosecond or even attosecond. Attosecond pulse enables time-domain access to electron dynamics, which is the fundamental driving force for atomic and molecular processes, including chemical reactions, ionization phenomena, and non-adiabatic dynamics [5–8]. The advantage of attosecond laser pulses has been used to measure lifetimes of the Auger decay process [9]. The lifetime quantity was deduced by a "streaking" analysis. But streaking method requires dedicated particle detection system and the streaking field may affect the dynamics to be measured [10]. After this, the decay of excited states of atoms after absorption of EUV light has been tracked via attosecond transient absorption (ATA) spectroscopy and lifetimes of autoionizing states have been determined [11,12]. However, the accuracy of the result is highly dependent on and limited by the energy resolution of the spectrometer [12].

Recently, transient wave-mixing spectroscopy, which is established on the base of nonlinear multidimensional spectroscopy in optical and radio frequency regime, has been developed to measure electronic dynamics [13–22]. In an attosecond wave-mixing measurement, there are usually three pulses, an attosecond EUV pulse for initiating electron dynamics followed by two NIR laser pulses for dynamics interrogation. The propagation direction and timing sequence of three pulses are variable. As a result, varity of wave-mixing designs have been explored for different measuring purposes [17–22]. For example, E. R. Warrick *et al.* studied the vibrational dynamics of dark state of N_2 by using different pulse timing sequences and beam direction geometries [19]. The lifetimes of dipole-allowed states of krypton atom have been retrieved in the work of A. P. Fidler *et al.* by using a geometry in which all three pulses are noncollinear and two delayed NIR pulses are coinciding in time [21].

In this work, we simulate the atomic helium interacting with three laser pulses in a noncollinear beam geometry, in which a co-propagating NIR/EUV pulse pair intersects with a delayed noncollinear few-cycle NIR pulse. Different phase matching channels lead to 8 dominating angle resolved wave-mixing signals, which carry rich information of the decaying dynamics of excited states. According to different temporal evolution characteristics, these emitting channels can be divided into two types: one mainly is the result of convolution of an exponential decayed function and a Gaussian function, from which the lifetime can be retrieved; the other is the superposition of convolutions of Gaussian functions and reflects the NIR pulse duration. By fitting the former type of wave-mixing signals, the accurate lifetimes of excited states with different parities can be successfully retrieved in a single measurement. This method eliminates the influence of detector energy resolution compared to existing ATA-based methods, and provides a superior time-domain measuring scheme for decaying dynamics.

2. Principle of measurement

As shown in Fig. 1, the noncollinear pulse geometry used in our method is composed of an attosecond EUV pulse, a few-cycle NIR pulse which is co-propagating with the EUV pulse along *y*-axis and another delayed NIR pulse intersecting with the other two pulses at a small angle θ in *xy*-plane. The EUV pulse has a Gaussian spatial distribution to mimic the real laser pulse in experiment while two NIR pulses are treated as plane waves considering that the beam spot of the NIR pulse is much bigger than that of the EUV pulse. All three pulses possess the same polarization direction (*z*-axis). In this design, the spatial distribution of helium atoms can be reduced to one dimension. In numerical calculations, we use 100 equally spaced grid points from -50 to 50 um along *x*-axis to represent the experimentally thin and uniform atomic distribution. As a result, the delayed NIR pulse reaches different grid points with different phases. The time-dependent polarization of helium atom located at each grid point has been calculated by solving a few-level time-dependent Schrödinger equation (TDSE) with the fourth-order Runge-Kutta method [23]. For simplicity, we only consider three essential states $1s^2$, $2s2p$ and $2p^2$ in the model, the autoionization effect due to the configuration interaction is included as decaying rates of the corresponding excited states in the Schrödinger equation (atomic units are used throughout the article unless otherwise specified) [24]:

$$i\partial_t \begin{pmatrix} C_g \\ C_a \\ C_b \end{pmatrix} = \begin{pmatrix} \omega_g & \mu_{ga}E & 0 \\ \mu_{ga}^*E^* & \omega_a - i\Gamma_a/2 & \mu_{ab}E \\ 0 & \mu_{ab}^*E^* & \omega_b - i\Gamma_b/2 \end{pmatrix} \begin{pmatrix} C_g \\ C_a \\ C_b \end{pmatrix},$$

(1)

where C_g, C_a and C_b are the time-dependent complex expansion coefficients of $1s^2$, $2s2p$ and $2p^2$ states of helium, while ω_g, ω_a and ω_b are the corresponding bare atom eigen-energies. μ_{ij} ($i = g, a, b$; $j = g, a, b$) represent dipole-moment matrix elements. E is the external electric

field consisting of EUV and NIR pulses. Γ_a and Γ_b are the decay rates of $2s2p$ and $2p^2$ states, respectively. The lifetime of an excited state has a relationship with its decay rate as $T = 1/\Gamma$. Note that the possible mechanisms such as autoionizing and decoherence that lead to decaying dynamics are not included explicitly in the model simulation. However, since the quantity that is investigated is the overall decaying rate of a specific excited state, the current simulation is appropriate for the general purpose of lifetime retrieval, and should not be restricted by specific decaying mechanisms [12,21]. In our simulation, the peak intensity of two NIR pulses is 2×10^{12} W/cm^2. The central wavelength of the NIR pulses is 642 nm, which is resonant with the $2s2p$-$2p^2$ transition. Attosecond EUV pulse has a peak intensity of 1×10^{10} W/cm^2 and centers at 60.15 eV. The full width at half maximum of the EUV pulse is 170 as, which can give an instantaneous excitation to the system. The intersection angle θ is set to be $4°$. More detailed information of the parameters can be found in Ref. [23]. Using this few-level model for each grid points, the corresponding space- and time-dependent dipoles can be calculated. Near-field nonlinear signals can be accessed from the Fourier transforms of these time-dependent dipoles [25]. Finally, the far-field energy- and divergence-angle-dependent emitting intensity can be obtained by using Fraunhofer diffraction equation for the near-field nonlinear signal. The delay-dependent signal intensity can be accessed by repeating the above processes for each delay.
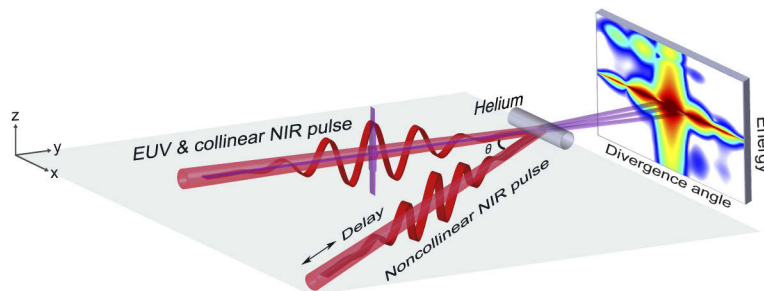
Fig. 1. Schematic diagram of the attosecond wave-mixing spectroscopy for lifetime detection. Attosecond EUV pulse copropagates with a beam of a few-cycle NIR pulse (collinear NIR pulse) along *y*-axis. The delayed few-cycle NIR pulse (noncollinear NIR pulse) intersects with the copropagated EUV/NIR pulse pair at a small angle θ. Helium atoms are located at the intersection of three pulses. The polarizations of three pulses are along the same direction, *z*-axis. The spatial intensity distribution of the EUV pulse is considered as Gaussian. Helium atoms are linearly arranged along the *x*-axis. The far-field spectrum is obtained by using Fraunhofer diffraction equation.

Figure 2 shows the energy and angle resolved far-field signal at zero delay. According to different energies and divergence angles, eight channels, named as channels 1 to 8, have been selected as shown in Fig. 2 for further discussion. The relative intensities between these channels differs remarkably, but they are spatially well separated and thus are detectable in a practical experiment. Besides, there are some experiments in which absorbance has been used to enlarge the relatively weak emitting signals [21].

Figures 3(a)-(h) are the phase matching geometries of the eight channels as shown in Fig. 2. Channels 2 and 4 are two six-wave mixing pathways, while the other channels are four-wave mixing processes. Note that only the lowest nonlinear order, which is the dominant process, is considered for each pathway. For channel 1, there are two possible geometries as shown in Fig. 3(a). The difference between them is the sequence of emitting a noncollinear and absorbing a collinear NIR photon. But absorbing a collinear NIR photon first is more probable since the $2s2p$ and $2p^2$ states are resonantly coupled with NIR pulse. As a result, the emitting signal of channel 1 mainly comes from the pathway shown in the right half of Fig. 3(a). This conclusion is also
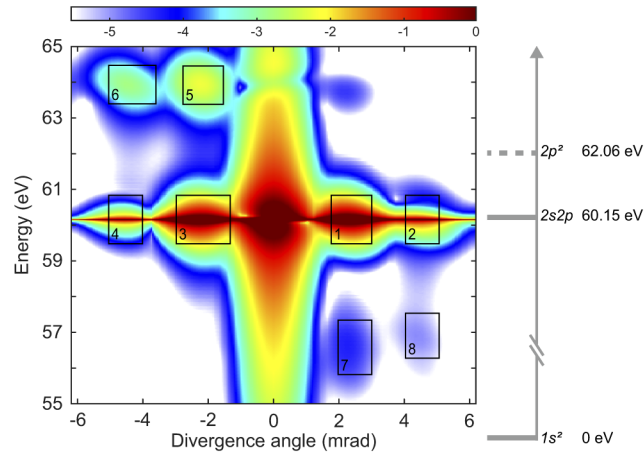
Fig. 2. Logarithmic spectral intensity as a function of photon energy and emitting divergence angle. Channels 1 to 8 are spectrally and spatially well separated. The energies of $2s2p$ and $2p^2$ states of helium atom are shown in the right of the figure.

applicable for the analysis of other channels except for channels 5 and 7. In terms of radiation intensity, the nonlinear signals from channels 1-4 are much stronger than that of channels 5-8 since the nonlinear interactions are mediated by the $2s2p$-$2p^2$ resonant transition. As for the emitting energy of these channels, Fig. 3 indicates that channels 1-4 possess the same emitting energy as $2s2p$ eigenenergy, and channels 5 and 6 locate at two NIR photon energy above the $2s2p$ level while channels 7 and 8 locate at two NIR photon energy below the $2s2p$ level, which is consistent with the result shown in Fig. 2.
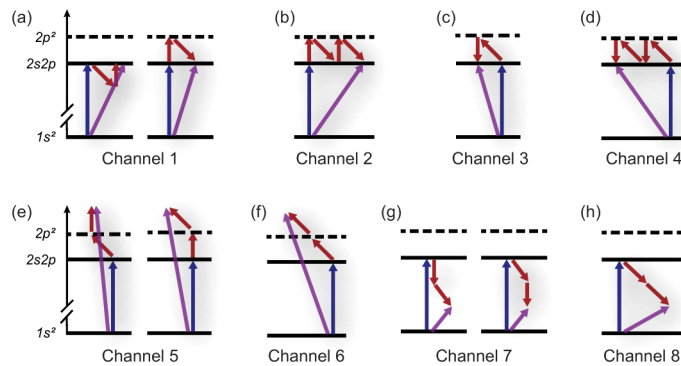
Fig. 3. Phase matching geometries of wave-mixing channels in Fig. 2. (a)-(h) are corresponding to channels 1-8, respectively. The solid horizontal black lines represent the ground and $2s2p$ states of helium while the black dashed lines represent the $2p^2$ dark states. Blue arrows mean the EUV photons. Red vertical arrows represent the collinear NIR photons and red inclined arrows are on behalf of noncollinear NIR photons. The purple arrows indicate the emitted EUV photons.

Different from the ATA, the radiation dipoles do not interfere with the EUV field. For a four-wave mixing process, the emitting signal intensity is proportional to the third-order polarization response function [4], which reads

$$|E_{\text{Emit}}|^2 \propto \left|P^{(3)}(\tau)\right|^2, \tag{2}$$

where E_{Emit} is the electric field of the third-order nonlinear signal. $P^{(3)}(\tau)$ is the delay dependent third-order polarization response function, while τ is the time-delay between the noncollinear NIR pulse and the co-propagating NIR/EUV pulse pair. Here, we choose channels 1 and 6 to derive the corresponding response function. In the semi-implusive limit, where the laser pulses are assumed to be short compared with any time scale of the system but long compared to the oscillation period of the light field, the third-order polarization for channel 1 can be written as [4]

$$
\begin{aligned}
\left|P_1^{(3)}(\tau)\right|^2 &= \int_0^\infty dt \left|P_1^{(3)}(t,\tau)\right|^2 \\
&\propto \int_0^\infty dt \left|\mu_{ga}^2 \mu_{ab}^2 e^{-i\omega_b\tau - \Gamma_b\tau/2} e^{-i\omega_a t - \Gamma_a t/2}\right|^2 \\
&= \mu_{ga}^4 \mu_{ab}^4 e^{-\Gamma_b\tau} \cdot \int_0^\infty dt \left|e^{-i\omega_a t - \Gamma_a t/2}\right|^2 \\
&= \frac{1}{\Gamma_a} \mu_{ga}^4 \mu_{ab}^4 e^{-\Gamma_b\tau}.
\end{aligned}
\tag{3}
$$

As for channel 6, a similar result can be derived:

$$
\begin{aligned}
\left|P_6^{(3)}(\tau)\right|^2 &= \int_0^\infty dt \left|P_6^{(3)}(t,\tau)\right|^2 \\
&\propto \int_0^\infty dt \left|\mu_{ga}^2 \mu_{ab}^2 e^{-i\omega_a\tau - \Gamma_a\tau/2} e^{-i\omega_c t - \Gamma_c t/2}\right|^2 \\
&= \mu_{ga}^4 \mu_{ab}^4 e^{-\Gamma_a\tau} \cdot \int_0^\infty dt \left|e^{-i\omega_c t - \Gamma_c t/2}\right|^2 \\
&= \frac{1}{\Gamma_c} \mu_{ga}^4 \mu_{ab}^4 e^{-\Gamma_a\tau}.
\end{aligned}
\tag{4}
$$

In the above equation, c denotes a laser dressed virtual state with energy one NIR photon energy above the $2p^2$ state. ω_c and Γ_c represent the energy and decay rate of the virtual state. Γ_i ($i = a, b$) is the reciprocal of lifetime T_i of the corresponding eigenstate. The emitting signal intensity can be written as

$$
\left|E_{\text{Emit,i}}\right|^2 \propto e^{-\tau/T_i}.
\tag{5}
$$

Equation (5) indicates that the lifetime of $2s2p$ (odd) or $2p^2$ (even) excited states can be accessed from the corresponding delay-dependent four-wave mixing channels. Other than the above mentioned two wave-mixing channels, it can be found that the delay-dependent emitting signal of channel 5 (channel 8) also contains the decaying dynamics of $2p^2$ ($2s2p$) state.

3. Result and discussion

3.1. Off-axis signal for lifetime retrieval

All these eight channels shown in Fig. 3 can be divided into two categories: the first type including channels 1, 5, 6 and 8 can be used for the lifetime retrieval; the second type including channels 2-4 and 7 reflects the information about NIR pulse duration. For these lifetime-detection channels, we can determine whose lifetime can be retrieved by pinpointing the state initially prepared by the NIR/EUV pulse pair. For example, as shown in the right half of Fig. 3(a), the NIR/EUV pulse pair gives $2p^2$ state an initial population. After excitation, $2p^2$ state decays with time and can be interrogated by a delayed noncollinear NIR pulse. Thus, the lifetime of $2p^2$ state can be extracted from the wave-mixing signal of channel 1. As for channel 6, the EUV pulse initially populates the $2s2p$ state promptly followed by a two-photon transition from the noncollinear NIR pulse. In this case, the lifetime of the $2s2p$ state is encoded in the wave-mixing signal.

Figure 4(a) is the delay dependent signal intensity of channels 1-8 integrated from specific energy and angle ranges shown in Fig. 2. In the numerical calculation, the decay rate of $2p^2$ state, Γ_b, is set to 100 meV, corresponding to the lifetime of 6.5 fs. The actual lifetime of helium $2p^2$ state is 108.3 fs [26]. We used a relatively shorter lifetime here to verify the generality of our model. To focus on the measurement of $2p^2$ dark state lifetime, the decay rate of $2s2p$ state, Γ_a, is set to 0. The positive delay corresponds to the condition when the EUV/NIR pulse pair leads the delayed NIR pulse. The result shows that the temporal evolution of channel 1 can be fitted by the convolution of a Gaussian function and an exponentially decaying function as shown in Fig. 4(b). According to Eq. (5), this fitted lifetime, T_1, is associated with the lifetime of $2p^2$ state. The fitted lifetime of $2p^2$ state is 6.4 fs. The variance of the fitting is on the order of 10^{-5}. Thus, the accurate lifetime of $2p^2$ dipole-forbidden state can be successfully retrieved from the wave-mixing signal of channel 1.
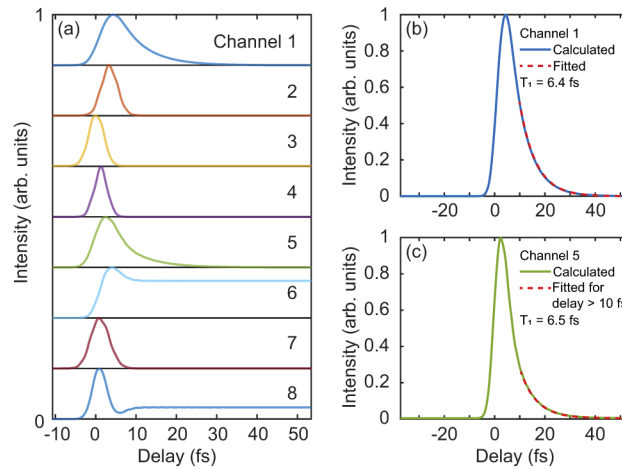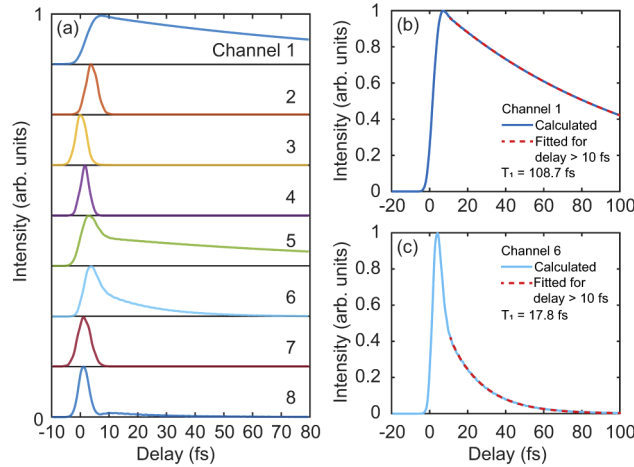

Fig. 4. (a) The delay dependent signal intensity of channels 1 to 8 when the decay rates of $2p^2$ and $2s2p$ states are 100 meV and 0 meV, respectively. (b) and (c) depict the calculated and fitted delay dependent signal intensity of channels 1 and 5, respectively.

Channel 5 can also be used for the lifetime detection of $2p^2$ state. The signal of a single wave-mixing channel like channel 5 comes from different quantum pathways [see Fig. 3(e)]. In order to fulfill the coherent interference, the final emitting energies and angles need to coincide simultaneously for different quantum pathways in a non-collinear wave-mixing geometry. The slight difference in either the final emitting energies or angles between different pathways makes the delay-dependent emitting signal show the property of incoherent superposition. An assumption has been made that the emitting signal of channel 5 is a linear combination of a Gaussian function and a Gaussian-exponential convolution function. To verify this, we use a linear combination of these two functions to fit the calculated curve. The fitted exponential decaying function has a time constant of 6.5 fs, which agrees with the 6.5-fs lifetime of the $2p^2$ state in the numerical calculation [see Fig. 4(c)]. And the proportion of the two fitting functions is close to 1: 1. It means that the two pathways have equal probability, which is in line with the fact that both pathways are double resonance four-wave mixing process. In summary, by analyzing the delay dependent emitting signal of channel 5, both the lifetime of $2p^2$ state and the contribution of the two involved pathways can be accessed. We can find that the emitting signals of channels 6 and 8 in Fig. 4 remain constant at large delays, indicating a zero decay rate for $2s2p$ state.

In a more general case, both the dark and bright states can decay simultaneously. Figure 5 shows the delay dependent signal intensities of channels 1-8 when the decay rates of both $2s2p$

and $2p^2$ states are considered, which are 37 meV and 6 meV, respectively [8]. The corresponding lifetimes of $2s2p$ and $2p^2$ states are 17.6 fs and 108.3 fs, respectively. Fitting the signal of channel 1 for delay beyond 10 fs gives a retrieved lifetime of 108.7 fs for the $2p^2$ state [see Fig. 5(b)]. Using the same fitting method, the lifetime of $2s2p$ state can also be extracted with high accuracy from channel 6 [see Fig. 5(c)]. We also successfully extracted the lifetime of $2p^2$ state from signal of channel 5. Theoretically, the signal of channel 8 can also be utilized for the lifetime retrieval of $2s2p$ state like channel 6, but channel 8 is much weaker than channel 6 and is modified and influenced by neighboring channels.

Fig. 5. (a) The delay dependent signal intensity of channels 1 to 8 when the decay rates of $2p^2$ and $2s2p$ states are 6 meV and 37 meV, respectively. (b) and (c) depict the calculated and fitted delay dependent signal intensity of channels 1 and 6, respectively.

In order to check the validity of our method, we performed additional calculations including $1s^2$, $2s^2$ (57.79 eV), $2s2p$ (60.15 eV), $2p^2$ (62.06 eV) and $2s3p$ (63.66 eV) states [26]. The results show that the lifetimes of doubly excited states can still be extracted correctly by fitting the emitting signals. We also fitted the wave-mixing signals of Fig. 4 and 5 for other delay ranges: delay beyond 15 fs and 20 fs. The results show that the fitting procedure using a constrained delay window does not influent the retrieved lifetime within the uncertainty of 1.5 %. In general, the decay of $2s2p$ and $2p^2$ state does not mutually affect the measurement of the lifetime of the individual state, precise and reliable lifetimes of states with both odd and even parities can be retrieved by using this wave-mixing method within a single measurement.

In Fig. 4 and 5, the second type channels including channels 2-4 and 7 show similar delay dependent structure: the emitting signal only exists when the two NIR pulses overlap. Although they cannot be utilized for lifetime detection, their temporal evolutions contain other dynamic information which will be discussed below.

3.2. Temporal evolution of wave-mixing channels

In Fig. 4 and 5, the signals from different channels emerge at different time delays and the maxima are also located at different delays. Here, we choose channels 2, 3 and 4 for a representative comparison to uncover the temporal evolution dynamics of different wave-mixing processes. Channel 3 and 4 possess the same emitting photonenergy and the emitting angle of channel 4 is twice of that in channel 3, that is, channel 4 is a higher order wave-mixing process than channel 3. The signal of channel 4 peaks at 1.5 fs after the maximum of signal of channel 3 [Fig. 6(a)]. This phenomenon also appeared in the wave-mixing experiments of helium and was attributed to the

real-time differences in the temporal dynamics of wave-mixing signal generation: channels with different orders are formed at different times during the nonlinear interaction [22]. It should be noticed that the experiment in [22] is conducted for singly excited sates of helium atoms, while our simulation is focusing on the doubly excited states with a simplified few-level model.
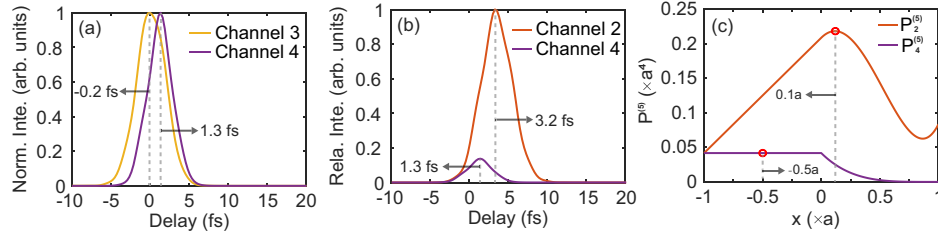
Fig. 6. Temporal evolution of wave-mixing channels with different nonlinear orders (a) and the same nonlinear order (b). (a) Delay-dependent normalized intensity of channels 3 (peaking at -0.2 fs) and 4 (peaking at 1.3 fs). (b) Relative intensity of channels 2 (peaking at 3.2 fs) and 4. The gray dashed lines indicate the locations of emitting peaks. (c) The graphical presentation of Eq. (7). The red circles represent the peak positions.

We find that not only there is an evolution difference between different wave-mixing orders, there is also evolution difference existing between channels with the same nonlinear order. For example, channels 2 and 4 are both six-wave mixing channels except that the sequence of absorbing and emitting collinear and noncollinear NIR photons is different as shown in Fig. 3(b) and (d). The peaks of both channels appear at positive time delays due to the causality of wave-mixing process [see Fig. 6(b)] [26]. For a six-wave mixing process, the emitted field (E_{Emit}) is proportional to the fifth-order polarization response function, $P^{(5)}(\tau)$. The corresponding response functions for channels 2 and 4 can be defined as:

$$P_2^{(5)}(\tau) \propto \mu_{ga}^2 \mu_{ab}^4 \int_0^{t_0} E_n dt_1 \int_0^{t_1} E_c dt_2 \int_0^{t_2} E_n dt_3 \int_0^{t_3} E_c dt_4,$$
$$P_4^{(5)}(\tau) \propto \mu_{ga}^2 \mu_{ab}^4 \int_0^{t_0} E_c dt_1 \int_0^{t_1} E_n dt_2 \int_0^{t_2} E_c dt_3 \int_0^{t_3} E_n dt_4. \qquad (6)$$

In the above equation, E_n and E_c represent the envelopes of noncollinear and collinear NIR pulses and the rotating wave approximation (RWA) has been used [27]. The EUV pulse is treated as Dirac delta function. To get an analytical solution of the response function, two NIR pulses are represented by rectangular pulses with duration T for simplicity. The collinear NIR pulse is centered at time zero synchronized with the EUV pulse, while the noncollinar NIR pulse is centered at τ. Solving Eq. (6) piecewise, the result is:

$$P_2^{(5)}(x) \propto \begin{cases} \frac{1}{24}a^4 + \frac{1}{6}a^3(x+a), & -a \leq x < 0 \\ \frac{7}{24}x^4 + \frac{a}{6}x^3 - \frac{3a^2}{4}x^2 + \frac{a^3}{6}x + \frac{5}{24}a^4, & 0 \leq x \leq a \end{cases}$$
$$P_4^{(5)}(x) \propto \begin{cases} \frac{1}{24}a^4, & -a \leq x < 0 \\ \frac{1}{24}x^4 - \frac{a}{6}x^3 + \frac{a^2}{4}x^2 - \frac{a^3}{6}x + \frac{1}{24}a^4, & 0 \leq x \leq a \end{cases} \qquad (7)$$

where $a = T/2$ and $x = \tau - a$. In the above equation, the response function only for $-a \leq x \leq a$ has been derived, for $x < -a$ and $x > a$, the nonlinear response drops to zero abruptly. As shown in Fig. 6(c), the maximum of $P_2^{(5)}(x)$ is located at $x = 0.1a$ ($\tau = 0.55T$) and the calculated $P_4^{(5)}(x)$ is constant in the region $-a \leq x < 0$. In order to quantify the peak position of $P_4^{(5)}(x)$, we choose the center of the region ($x = -0.5a$), that is, $\tau = 0.25T$, as the peak location of $P_4^{(5)}(x)$. In the

simulation of Fig. 6(b), T is roughly equal to 6 fs. According to Eq. (7), the signal of channels 2 and 4 should peak at 3.3 and 1.5 fs, respectively, which is roughly consistent with the simulated result [Fig. 6(b)]. The derivation of Eq. (7) based on RWA ignored the extended spectrum of the rectangular NIR pulse and is only a rough qualitative evaluation of the temporal evolution of different wave-mixing channels. The phenomenon that the intensity and temporal evolution of the two channels differ remarkably from each other shows that these six-wave mixing channels are highly photon-sequence-dependent.

The signal of channel 2 in Fig. 6(b) has a small shoulder at approximately 7 fs. And other channels in Fig. 6 also show similar structures. This is closely related to the contribution from other higher order non-resonant wave-mixing pathways. The signals shown in Fig. 6 are only generated when all three pulses overlap in time. Therefore, they do not provide any lifetime information but rather reflect the convolution profile between the two NIR pulses.

3.3. On-axis absorption spectrum for waveform measurement

Not only does the off-axis wave-mixing signal reveal important dynamic information, the on-axis signal can also be used for the measurement of ultrafast process. In our previous work, we demonstrated an all-optical method for time-domain characterization of ultrashort optical pulses using a three-pulse configuration [23]. A moderately intense laser pulse couples the doubly excited states of helium and induces the ac Stark effect. A synchronized weak signal field perturbs the coupling process and alters the quasienergies of the dressed atom, upon which the carrier oscillation of the signal field is encoded. The EUV pulse plays the role of a transient probe to get the quasienergies of excited states. But all three pulses are collinear in Ref. [23], and as a result, long tails exist and persist at larger delays in the extracted waveform due to quantum pathway interference. To utilize the advantage of a noncollinear wave-mixing spectroscopy where signals from different quantum channels separate in space, we tried to implement the waveform sampling of a few-cycle optical pulse by using the present noncollinear wave-mixing design. To get a visible splitting of the $2s2p$ state, the intensity of collinear NIR pulse is set to 6×10^{12} W/cm^2. Figure 7(a) is the on-axis absorption spectrum when the intersection angle, θ, is 1°. The tail at large delays (>10 fs) is still distinct. Figure 7(b) shows the condition when θ is equal to 2° and noncollinear NIR intensity is four times of that in Fig. 7(a). The tail at large delays has been greatly reduced. This noncollinear geometry can eliminate the long-existed tail in the extracted waveform after the pulse duration in the collinear geometry, which greatly improves the performance of our previous waveform sampling method.
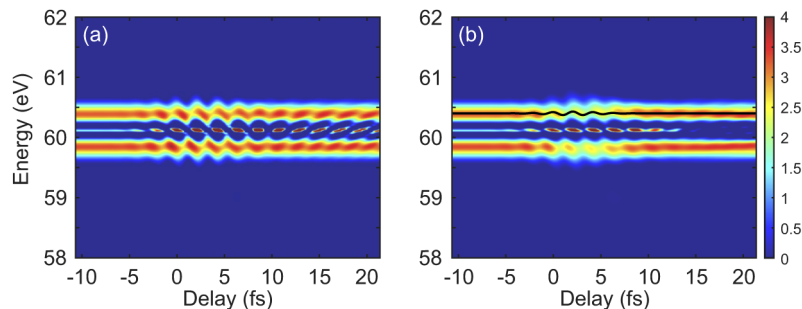
Fig. 7. On-axis absorption spectrum. (a) is the result when the intersection angle between noncollinear NIR pulse and EUV/NIR pulse pair is 1°. (b) is the result when the intersection angle is 2° and the noncollinear NIR peak intensity is four times of the intensity in (a). Black curve is the incident pulse electric field.

4.   Conclusion

In summary, we have proposed a versatile method for accurately measuring the lifetimes of excited states based on attosecond wave-mixing spectroscopy. By using well-selected wave-mixing geometry and pulse sequence, this method can retrieve the lifetimes of states with both odd and even parities simultaneously. The error is on the order of a few hundred attoseconds and the relative error is within 1.5 %. The accuracy of this method should be mainly limited by the waveform stability, jittering of the pulse, pulse energy fluctuation and the signal-to-noise ratio when a real experiment is conducted. Thanks to the channel-resolved capability of the method, the temporal evolution dynamics of multiple channels can be tracked. The numerical analysis reveals that the emitting signal is sensitive to the wave-mixing order. In addition, we find that for channels with the same wave-mixing order, their intensity and temporal evolution still differ greatly from each other. This means that the wave-mixing process is highly photon-order-dependent. Besides, in the same measurement, the on-axis absorption spectrum can be used for the optical waveform sampling and eliminates the errors caused by the quantum pathways interference, which means that both off- and on-axis signals in this wave-mixing scheme can be used for high precision diagnosis of ultrafast processes. The current method provides a versatile and reliable tool for the study of excited state decaying dynamics, which will aid the investigation of state-resolved dynamics in time domain.

Disclosures. The authors declare no conflicts of interest.

References

1. M. K. Odling-Smee, E. Sokell, P. Hammond, and M. A. MacDonald, "Radiative decay of doubly excited states in helium below the he$^+$ (N=2) ionization threshold," Phys. Rev. Lett. **84**(12), 2598–2601 (2000).
2. U. Fano, "Effects of configuration interaction on intensities and phase shifts," Phys. Rev. **124**(6), 1866–1878 (1961).
3. D. L. Ederer, "Cross-section profiles of resonances in the photoionization continuum of krypton and xenon (600-400 å)," Phys. Rev. A **4**(6), 2263–2270 (1971).
4. S. Mukamel, *Principles of Nonlinear Optical Spectroscopy* (Oxford University Press, New York, 1995).
5. F. Krausz and M. Ivanov, "Attosecond physics," Rev. Mod. Phys. **81**(1), 163–234 (2009).
6. A. R. Beck, D. M. Neumark, and S. R. Leone, "Probing ultrafast dynamics with attosecond transient absorption," Chem. Phys. Lett. **624**, 119–130 (2015).
7. A. Föhlisch, P. Feulner, F. Hennies, A. Fink, D. Menzel, D. Sanchez-Portal, P. Echenique, and W. Wurth, "Direct observation of electron dynamics in the attosecond domain," Nature (London) **436**(7049), 373–376 (2005).
8. C. Ott, A. Kaldun, L. Argenti, P. Raith, K. Meyer, M. Laux, Y. Zhang, A. Blättermann, S. Hagstotz, T. Ding, R. Heck, J. Madroñero, F. Martín, and T. Pfeifer, "Reconstruction and control of a time-dependent two-electron wave packet," Nature (London) **516**(7531), 374–378 (2014).
9. M. Drescher, M. Hentschel, R. Kienberger, M. Uiberacker, V. Yakovlev, A. Scrinzi, T. Westerwalbesloh, U. Kleineberg, U. Heinzmann, and F. Krausz, "Time-resolved atomic inner-shell spectroscopy," Nature **419**(6909), 803–807 (2002).
10. W.-C. Chu and C. D. Lin, "Theory of ultrafast autoionization dynamics of fano resonances," Phys. Rev. A **82**(5), 053415 (2010).
11. H. Wang, M. Chini, S. Chen, C.-H. Zhang, F. He, Y. Cheng, Y. Wu, U. Thumm, and Z. Chang, "Attosecond time-resolved autoionization of argon," Phys. Rev. Lett. **105**(14), 143002 (2010).
12. B. Bernhardt, A. R. Beck, X. Li, E. R. Warrick, M. J. Bell, D. J. Haxton, C. W. McCurdy, D. M. Neumark, and S. R. Leone, "High-spectral-resolution attosecond absorption spectroscopy of autoionization in xenon," Phys. Rev. A **89**(2), 023408 (2014).
13. S. Mukamel, "Femtosecond optical spectroscopy: A direct look at elementary chemical events," Annu. Rev. Phys. Chem. **41**(1), 647–681 (1990).
14. P. Hamm and M. Zanni, *Concepts and methods of 2D infrared spectroscopy* (Cambridge University, Cambridge, 2011).
15. M. Dantus, "Coherent nonlinear spectroscopy: From femtosecond dynamics to control," Annu. Rev. Phys. Chem. **52**(1), 639–679 (2001).
16. S. Mukamel, D. Healion, Y. Zhang, and J. D. Biggs, "Multidimensional attosecond resonant x-ray spectroscopy of molecules: Lessons from the optical regime," Annu. Rev. Phys. Chem. **64**(1), 101–127 (2013).

17. W. Cao, E. R. Warrick, A. Fidler, S. R. Leone, and D. M. Neumark, "Near-resonant four-wave mixing of attosecond extreme-ultraviolet pulses with near-infrared pulses in neon: Detection of electronic coherences," Phys. Rev. A **94**(2), 021802 (2016).

18. W. Cao, E. R. Warrick, A. Fidler, D. M. Neumark, and S. R. Leone, "Noncollinear wave mixing of attosecond XUV and few-cycle optical laser pulses in gas-phase atoms: Toward multidimensional spectroscopy involving xuv excitations," Phys. Rev. A **94**(5), 053846 (2016).

19. E. R. Warrick, A. P. Fidler, W. Cao, E. Bloch, D. M. Neumark, and S. R. Leone, "Multiple pulse coherent dynamics and wave packet control of the N_2 a" $^1\Sigma_g^+$ dark state by attosecond four-wave mixing," Faraday Discuss. **212**, 157–174 (2018).

20. H. J. B. Marroux, A. P. Fidler, D. M. Neumark, and S. R. Leone, "Multidimensional spectroscopy with attosecond extreme ultraviolet and shaped near-infrared pulses," Sci. Adv. **4**(9), eaau3783 (2018).

21. A. P. Fidler, H. J. B. Marroux, E. R. Warrick, E. Bloch, W. Cao, S. R. Leone, and D. M. Neumark, "Autoionization dynamics of (2P1/2)ns/d states in krypton probed by noncollinear wave mixing with attosecond extreme ultraviolet and few-cycle near infrared pulses," J. Chem. Phys. **151**(11), 114305 (2019).

22. A. P. Fidler, S. J. Camp, E. R. Warrick, E. Bloch, H. J. Marroux, D. M. Neumark, K. J. Schafer, M. B. Gaarde, and S. R. Leone, "Nonlinear XUV signal generation probed by transient grating spectroscopy with attosecond pulses," Nat. Commun. **10**(1), 1384–1388 (2019).

23. K. Mi, W. Cao, H. Xu, Y. Mo, Z. Yang, P. Lan, Q. Zhang, and P. Lu, "Perturbed ac stark effect for attosecond optical-waveform sampling," Phys. Rev. Appl. **13**(1), 014032 (2020).

24. Y. Kobayashi, H. Timmers, M. Sabbar, S. R. Leone, and D. M. Neumark, "Attosecond transient-absorption dynamics of xenon core-excited states in a strong driving field," Phys. Rev. A **95**(3), 031401 (2017).

25. M. B. Gaarde, C. Buth, J. L. Tate, and K. J. Schafer, "Transient absorption and reshaping of ultrafast XUV light by laser-dressed helium," Phys. Rev. A **83**(1), 013419 (2011).

26. V. Stooß, S. M. Cavaletto, S. Donsa, A. Blättermann, P. Birk, C. H. Keitel, I. Březinová, J. Burgdörfer, C. Ott, and T. Pfeifer, "Real-time reconstruction of the strong-field-driven dipole response," Phys. Rev. Lett. **121**(17), 173005 (2018).

27. M. Chini, X. Wang, Y. Cheng, and Z. Chang, "Resonance effects and quantum beats in attosecond transient absorption of helium," J. Phys. B **47**(12), 124009 (2014).